On-chip diamond MEMS magnetic sensing through multifunctionalizing magnetostrictive thin film

Zilong Zhang[1], Wen Zhao[2], Guo Chen[1], Masaya Toda[3], Satoshi Koizumi[1], Yasuo Koide[1], Meiyong Liao[1*]

[1] Research Center for Functional Materials, National Institute for Materials Science (NIMS), 1-1 Namiki, Tsukuba, Ibaraki 3050044, Japan

[2] Physical Sciences and Engineering Division, King Abdullah University of Science and Technology, Thuwal, Saudi Arabia

[3] Graduate School of Engineering, Tohoku University, Sendai, Miyagi 9808579, Japan

Correspondence should be addressed to Meiyong Liao* (Email: meiyong.liao@nims.go.jp)

Abstract

Electrically integrable, high-sensitivity, and high-reliability magnetic sensors have not yet been realized at high temperatures (500 °C). In this study, we demonstrate an integrated on-chip single-crystal diamond (SCD) micro-electromechanical system (MEMS) magnetic transducer by coupling SCD with a large magnetostrictive FeGa film. The FeGa film is multifunctionalized to actuate the resonator, self-sense the external magnetic field, and electrically read the resonance signal. The on-chip SCD MEMS transducer shows a high-sensitivity of 3.2 Hz/mT from room temperature to 500 °C and a low noise level of 9.45 nT/Hz$^{1/2}$ up to 300 °C. The minimum fluctuation of the resonance frequency is 1.9×10^{-6} at room temperature and 2.3×10^{-6} at 300 °C. An SCD MEMS resonator array with parallel electric readout is subsequently achieved, thus providing a basis for the development of magnetic image sensors. The present study facilitates the development of highly integrated on-chip MEMS resonator transducers with high performance and high thermal stability.

Keywords: Single-crystal diamond, MEMS, on-chip actuation and sensing, magnetic sensor

1. Introduction

Real-time health care of human beings for Internet of Things, precise biomedical diagnosis, and infrastructure maintenance, particularly under extreme conditions, increases the immediate demand for developing integrated magnetic sensing technology with high sensitivity, high reliability, low power consumption, and minimized size.[1-8] The current magnetic sensors primarily include superconducting quantum interference device (SQUID) sensors, Hall sensors, fluxgate sensors, magneto-resistive (MR) sensors, nitrogen-vacancy (NV) sensors, and micro-electromechanical system (MEMS) sensors.[2, 9-14] The SQUID sensors with the highest magnetic resolution of fT level require high cost and liquid nitrogen/helium as a refrigerant, which render them less advantageous compared with other magnetic sensors.[15] For Hall sensors, their low sensitivity and resolution limit their performance and applications.[14] Fluxgate sensors require complex processes to fabricate their magnetic cores and coils, which feature large masses and high power consumption.[16] The restricted magnetic field magnitude appearance of MR sensors suppresses their application regimes.[17] Another promising magnetic sensor is based on the NV center in diamond, which in principle shows high sensitivity and nanoscale resolution. However, the controllability of the NV center and the electrical readout of NV signals are challenging.[18-20] MEMS technology exhibits the merits of batch fabrication, controllability in dimensions down to the nanoscale, low power consumption, low cost, high sensitivity, and high integration.[21]

In addition, for harsh application fields such as mineral/oil exploration, space exploration, high-temperature magnetic valves, and engine and transmission speed control in cars, magnetic sensors with high thermal-stability performance are in high demand.[22, 23] Recently, the main high-temperature magnetic sensors, including MR sensors, fluxgate sensors, and Hall sensors, are affected by material and physical limitations under extreme conditions, which result in low sensitivity, weak thermal stability, and restrained operating temperatures.[24-26] MEMS resonators coupled with soft magnetic materials provide a new paradigm for fabricating various

magnetic transducers.[27, 28] Furthermore, a MEMS resonator array with high integration can be developed, which yields efficient and precise special mapping of magnetic fields.[29] To develop MEMS magnetic sensor arrays, all electrical actuation and sensing are necessary for integration with electronics.

Single-crystal diamond (SCD) is a promising material for high-performance and high-reliability MEMS devices owing to its outstanding physical, chemical, mechanical, and electrical properties.[30-42] SCD MEMS resonators combined with galfenol (FeGa), a material with a large magnetostrictive coefficient of 375 ppm and an ultrahigh Curie temperature of 675 °C, provide an ideal scheme for high-sensitivity and thermal-stability magnetic transducers *via* the delta-E (ΔE) effect.[43, 44] To achieve highly integrated high-sensitivity SCD MEMS transducers, all-electrical on-chip actuation and sensing are required.[45] The piezoelectric effect and electrostatic or dielectric actuation with capacitive sensing were developed to fulfill the functions of actuation and readout.[46-49] The piezoelectric method offers an efficient route with high electromechanical coupling efficiency, but the energy dissipation induced by the multilayer degrades the sensitivity. The dielectric actuation overcomes the energy dissipation problem, and an off-chip bulky optical readout was achieved.[50] For highly integrated MEMS magnetic sensors, a scheme with multiple functions including actuation, sensing, and signal readout is desired. In this study, we propose and demonstrate an on-chip SCD MEMS magnetic sensor by multifunctionalizing a magneto-strictive FeGa film for harmonic actuation, magnetic sensing, and resonance signal readout. To enhance adhesion at the interface between FeGa and the SCD, a Ti thin film was added to form a FeGa/Ti/SCD magnetic transducer. The magnetic transducer fulfilled magnetic transducing performance with high-temperature operation up to 500 °C, a sensitivity of 3.2 Hz/mT from room temperature to 500 °C, and a low noise level of 9.45 nT/Hz$^{1/2}$ at 300 °C. The fluctuation of the resonance frequency was 1.9×10^{-6} at room temperature and 2.3×10^{-6} at 300 °C. Furthermore, a prototype magnetic transducer array based on on-chip FeGa/Ti/SCD MEMS magnetic transducers was developed. This study provides a

promising strategy for developing highly integrated MEMS magnetic transducers with high performance and reliability, which are superior to the present magnetic transducers.

2. Results and Discussion

SCD cantilevers with an SCD-on-SCD structure provide a robust platform for fabricating MEMS magnetic transducers. The fabrication process of the SCD cantilever-based magnetic transducer is shown in **Figure S1 (Supporting Information)**. First, bare SCD cantilevers were fabricated via the smart-cut technique, which primarily includes carbon ion implantation, diamond growth, photolithography treatment, metal mask deposition, reactive ion etching, and structure release. The bare SCD cantilevers fabricated via this technique exhibit high reliability and high Q factors. The details of this approach for batch production are available in our previous publication.[51, 52] Subsequently, a 2-nm-thick Ti film followed by a 90-nm-thick FeGa film was deposited on the bare SCD cantilevers using a magnetron sputtering system, followed by a 1-nm-thick Ti film and a 7-nm-thick Au film using an e-beam evaporator system. The 90 nm FeGa thin film is a trade-off for the quality (Q) factor of the SCD resonator and the optimization of the magnetic properties of the FeGa thin film. The thick FeGa film resulted in a reduced Q factor, whereas the thin FeGa film degraded the magnetic properties.

2.1 Resonator elasticity vibration theory

The mechanical vibration characteristics of a rectangular uniform cantilever beam can be described and analyzed based on the Euler–Bernoulli law (**see the SI**).[53] The resonance frequency of the fundamental (first) mode is expressed as

$$f = 0.162 \frac{t_{th}}{L^2} \sqrt{\frac{E}{\rho}}, \quad (1)$$

where E and ρ are the Young's modulus and mass density of the beam, respectively; and L and t_{th} denote beam length and thickness, respectively. The resonance frequency is determined by the dimensions and material properties of the cantilever.

2.2 Self-sensing and actuation of cantilever resonance

In this study, Au/FeGa/Ti was deposited on the SCD substrate as the gate (G) electrode for on-chip actuation and on the SCD cantilevers as source–drain (S–D) electrodes to sense the magnetic fields and electrically readout the resonance signal. **Figure 1a** shows the actuation and readout circuits of the on-chip SCD resonator. The ultimate optical feature of a 160-μm-long SCD cantilever magnetic transducer is shown in **Figure 1b.** A radio-frequency (RF) signal with an amplitude of V_g^{ac} and a frequency of ω was applied to the G electrode. Another RF signal with an amplitude of V_{sd}^{ac} and a frequency of $\omega+\Delta\omega$ was connected to the S–D electrodes to read out the vibration signal. For a certain gate voltage V_g, a charge q was induced on the cantilever, which is expressed as $q = C_g V_g$, where C_g is the capacitance between the G electrode and cantilever. The electrostatic force results in the bending of the cantilever. In this study, $V_g = V_g^{ac} cos(\omega\tau)$. The total energy stored in the capacitor is $E_{eng}=1/2C_g(z)V_g^2$,[54] where z is the distance between the G electrode and cantilever. The total electrostatic force on the cantilever is expressed as[54]

$$F_{el} = \frac{\partial E_{eng}}{\partial z} = \frac{1}{2}\frac{dC_g}{dz}(V_g^{ac} cos\ \omega\tau)^2 \quad (2)$$

$V_g^{ac}\ cos(\omega\tau)$ results in a periodic electric force that causes the cantilever to vibrate. The displacement of the cantilever is the largest when the driving frequency is at its resonance frequency.

The signal readout resulting from the cantilever motion is based on the piezoresistive effect of the S–D electrode on the cantilever. To characterize the output signal, a modulation frequency $\Delta\omega$ of 5 kHz was set. The output signal generated at the S electrode is a mixture of signals from the G and D electrodes, which is expressed as[55, 56]

$$V_{out} = \frac{\Delta R_0}{R+R_0} V_{sd}^{ac}[cos(\Delta\omega\tau - \varphi) + cos((2\omega + \Delta w)\,\tau + \varphi)], \quad (3)$$

where R is the circuit resistance; R_0 is the resistance of the electrode deposited on the cantilever, which is approximately 100 Ω; V_{sd}^{ac} is the voltage applied to the S–D electrodes; and ΔR_0 represents the resistance change of the metal electrode on the cantilever owing to its vibration

motion. The bias signal mixes with the vibration motion of the metal electrode and generates signals at frequencies $\Delta\omega$ and $2\omega+\Delta\omega$. A low-pass filter was utilized to filter the frequency of $2\omega+\Delta\omega$. The remaining signals were fed into a lock-in amplifier for the readout. The output signal at a frequency of $\Delta\omega$ is expressed as

$$V_{out} = \frac{\Delta R_0}{R+R_0} V_{sd}^{ac} \cos(\Delta\omega\tau - \varphi) \quad (4)$$

The amplitude of the output voltage reached its maximum value when the cantilever vibrated at its resonance frequency. Thus, the SCD cantilever with the actuation and sensing structure can realize the actuation and detection of mechanical motion. This actuation and sensing scheme provides a strategy to design MEMS devices with an electrical interface for integration with electronics.

2.3 Magnetic sensing principle based on ΔE effect

For a magnetostrictive material, the Young's modulus changes during the magnetization process, which is known as the ΔE effect.[57, 58] The ΔE effect is expressed as

$$\Delta E = E_0 - E_H, \quad (5)$$

where E_0 and E_H are Young's moduli of the material without and with the application of a magnetic field, respectively. The ΔE effect of the ferromagnetic thin film deposited on the SCD cantilever is regarded as the magnetic sensing principle. **Figure 1c** schematically shows the fundamental sensing principle of the magnetic transducer based on the SCD cantilever structure. By applying an external magnetic field, the SCD cantilever is subjected to bending stress induced by the FeGa film. The shape of the FeGa film varies depending on the ΔE effect, which results in a change in its Young's modulus. Consequently, the effective Young's modulus of the SCD-based cantilever with multiple layers changes. Subsequently, the resonance frequency of the SCD-based cantilever shifts owing to the ΔE effect. The magnetic sensitivity of the SCD-based cantilever transducer is characterized as the resonance frequency response to the magnetic field.

2.4 Fundamental mechanical resonance

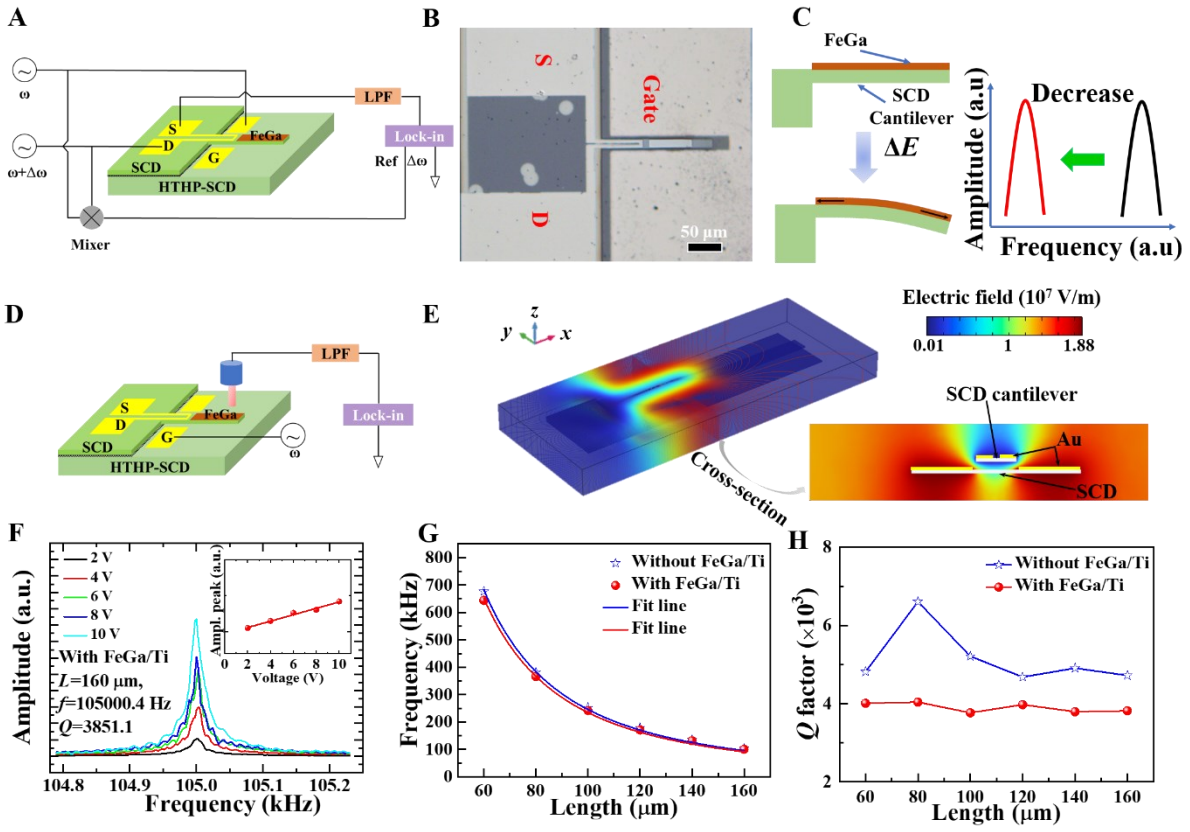

Figure 1. Measurement setup and resonance performances of the SCD-based resonators. A) Schematic diagram of the measurement setup for the SCD-based cantilever magnetic transducer with the on-chip self-sensing and actuation configuration. LPF: low frequency filter. B) Optical images of a 160-μm-long SCD-based cantilever magnetic transducer. C) Magnetic sensing principle of a cantilever resonator with resonance frequency shift. D) Schematic image of the measurement setup with an optical readout system. E) Simulation of the electric field distribution of a SCD-based resonator with on-chip actuation. S–D electrodes are grounded and V_g^{ac} = 1 V. F) Typical resonance frequency spectra of a 160-μm-long SCD-based cantilever. Inset shows the motion amplitude with linear dependence on the gate voltage. G) Resonance frequencies and H) Q factors of SCD-based cantilevers dependence on length L without and with deposition of FeGa/Ti film.

To investigate the harmonic oscillation characteristics of SCD-based cantilevers, the S–D electrodes were grounded and the G electrode was connected to an RF signal source. A laser Doppler vibrometer was utilized to analyze the harmonic signal of the SCD-based oscillator, as shown in **Figure 1d**.[51, 52] The electric field distribution of the SCD-based oscillator was

simulated using the COMSOL software as the S–D electrodes were grounded and V_g^{ac} = 1 V, which reflected the electric field confined around the SCD cantilever (**Figure 1e and Figure S2, Supporting Information)** The gate voltage did not significantly affect the resonance frequency (**Figure 1f**) and linearly enhanced the amplitude of the resonance spectrum (the inset of **Figure 1f**). The dependence of the resonance frequency on the length of the oscillator with and without the deposition of FeGa/Ti films is depicted in **Figure 1g**. The dependences of the resonance frequency of the SCD-based oscillator with and without FeGa/Ti films on the length agreed well with **Equation 1**. The *Q* factors of the SCD oscillators decrease after the deposition of the FeGa/Ti films (**Figure 1h** and **Equation S6, Supporting Information)** but remained as high as approximately 4000.

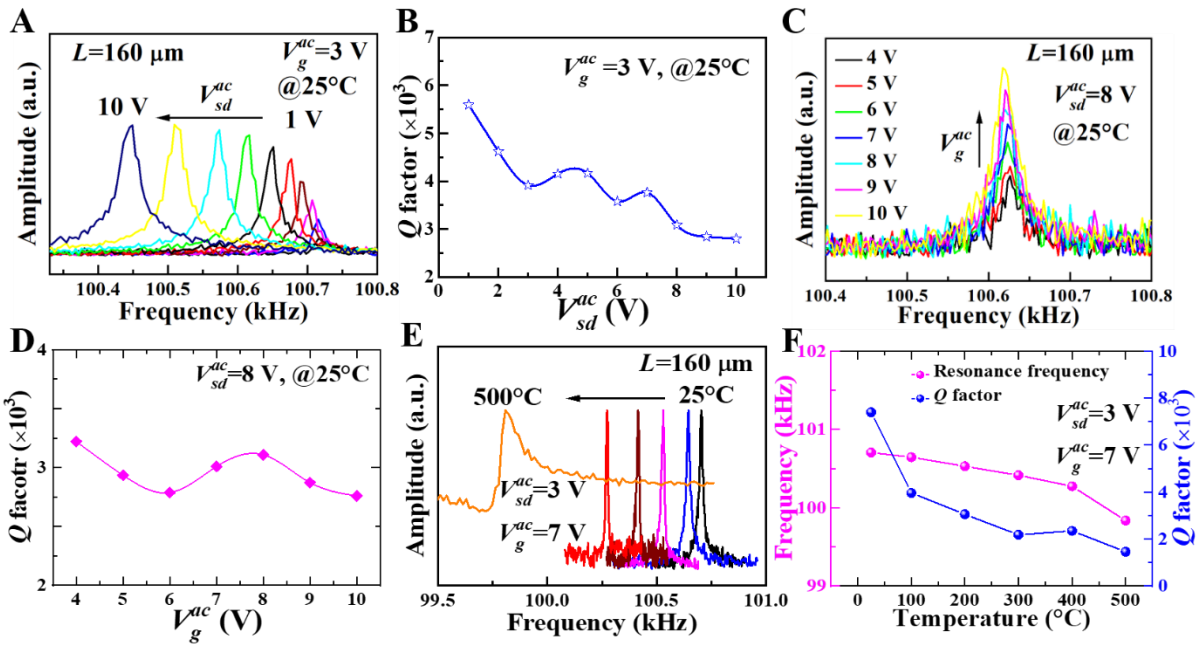

Figure 2. Resonance performances of the SCD-based cantilever transducer with on-chip actuation and sensing scheme. A) Resonance frequency spectra of a 160-μm-long SCD-based cantilever transducer measured by the electrical readout system at various V_{sd}^{ac} and V_g^{ac}=3 V @25 °C. The resonance frequency shifts downward as V_{sd}^{ac} increases. B) Dependences of *Q* factors on V_{sd}^{ac} at V_g^{ac}=3 V @25 °C. C) Resonance frequency spectra of a 160-μm-long SCD-based cantilever transducer measured by the electrical readout system at various V_g^{ac} and V_{sd}^{ac} = 8 V @25 °C. D) Variations in *Q* factors with V_g^{ac} at V_{sd}^{ac} = 8 V. E) Resonance frequency spectra of a 160-μm-long SCD-based cantilever transducer measured *via* the electrical readout system

194 from 25 °C to 500 °C at V_{sd}^{ac} = 3 V and V_g^{ac} = 7 V. F) Resonance frequencies and Q factors as a
195 function of temperature.
196
197 The measurement setup for the on-chip sensing and actuation of the SCD cantilevers
198 through an electrical system has been previously described **(Figure 1a)**. The resonance
199 frequency spectra of a 160-μm-long SCD-based oscillator were customized by changing V_{sd}^{ac} to
200 V_g^{ac} = 3 V at 25 °C, as shown in **Figure 2a**. The resonance frequency spectrum shifted downward
201 as V_{sd}^{ac} increased, whereas the resonance frequency amplitude increased with V_{sd}^{ac}. The reduction
202 in resonance frequency, which is known as the "softening" of the SCD-based oscillator, may
203 be attributed to two reasons:1) the existence of an electric field force gradient and 2) Joule
204 heating from the S–D electrodes. When an external electric field V_{sd}^{ac} is applied, the resonance
205 frequency of the cantilever oscillator can be expressed as $f \approx f_0 + \alpha (V_{sd}^{ac})^2/(mf_0)$,[59] where α is the
206 coefficient related to the SCD polarizability and electric field gradient, f_0 is the resonance
207 frequency of the oscillator without an electric field force, and m is the oscillator mass. The
208 resonance frequency exhibits a square relationship with V_{sd}^{ac}, as shown in **Figure S3**
209 **(Supporting Information)**. Furthermore, the inset of **Figure S3 (Supporting Information)**
210 shows that the ratio of the resonance frequency variation ($\Delta f = f - f_0$) to f_0 increases linearly with
211 $(V_{sd}^{ac})^2$. Meanwhile, the local temperature of the SCD cantilever increases with V_{sd}^{ac}, which
212 decreases the effective Young's modulus and thus induce a downward shift of the resonance
213 frequency. The function of the resonance frequency shift with the temperature coefficient of
214 Young's modulus is expressed as[60]

215 $$\frac{\Delta f}{f} \approx \frac{1}{2}\frac{\Delta E}{E} \approx \frac{1}{2}\alpha_E \frac{dT}{dW} W \propto (V_{sd}^{ac})^2, \quad (6)$$

216 wherein $\alpha_E = dE/(E dT)$; and W is the input electrical energy, which is proportional to $(V_{sd}^{ac})^2$.
217 Thus, $\Delta f/f$ exhibits a linear relationship with $(V_{sd}^{ac})^2$. The exact reason for the downward shift of
218 the resonance frequency of the cantilever oscillator is yet to be confirmed. The plot of the Q
219 factor *vs.* V_{sd}^{ac} is presented in **Figure 2b**, which shows that the Q factor decreases as V_{sd}^{ac} increases.

A more accurate analysis should consider the thermal mismatch between diamond and FeGa, which does not affect the magnetic sensitivity for a certain S–D voltage.

The resonance frequency spectra of the SCD-based resonator were characterized by varying V_g^{ac} at V_{sd}^{ac} = 8 V and room temperature (**Figure 2c**). The resonance frequency shifted downward as V_g^{ac} increased, as shown in **Figure S3 (Supporting Information)**. For a cantilever beam, the resonance frequency is determined by the uniaxial compressive stress, σ of the cantilever beam, which is expressed as[61]

$$f = f_0(1 + 0.295\frac{\sigma L^2}{Et^2})^{1/2} \quad (7)$$

According to **Equation 2**, σ can be increased by adopting a higher value of V_g^{ac}. Thus, the decrease in the resonance frequency with a higher V_g^{ac} indicates that σ is a tension stress. This is different from the case of the optical readout without applying an S–D voltage. The Q factor shows a weak dependence on V_g^{ac} (**Figure 2d**). The thermal stability of the resonance performance of the SCD-based oscillator was examined as the temperature increased from 25 °C to 500 °C. The temperature dependence of the resonance frequency spectra of the SCD-based oscillator is shown in **Figure 2e**. V_{sd}^{ac} and V_g^{ac} were fixed at 3 and 7 V, respectively. The temperature increase resulted in a decrease in the effective Young's modulus of the multilayer structure, which caused a downward shift in the resonance frequency (**Figure 2f**). Alternatively, the temperature coefficient of the resonance frequency (TCF) was used to demonstrate the thermal stability of the SCD-based oscillator (**Figure S4, Supporting Information**). The TCF of SCD-based oscillators with various lengths can remain lower than 13 ppm/K, which is superior to that of Si with a value of 35 ppm/K.[62] The Q factor of the SCD-based oscillator decreased at high temperatures but remained as high as 1500 even at 500 °C.

2.5 Magnetic transducing at high temperatures

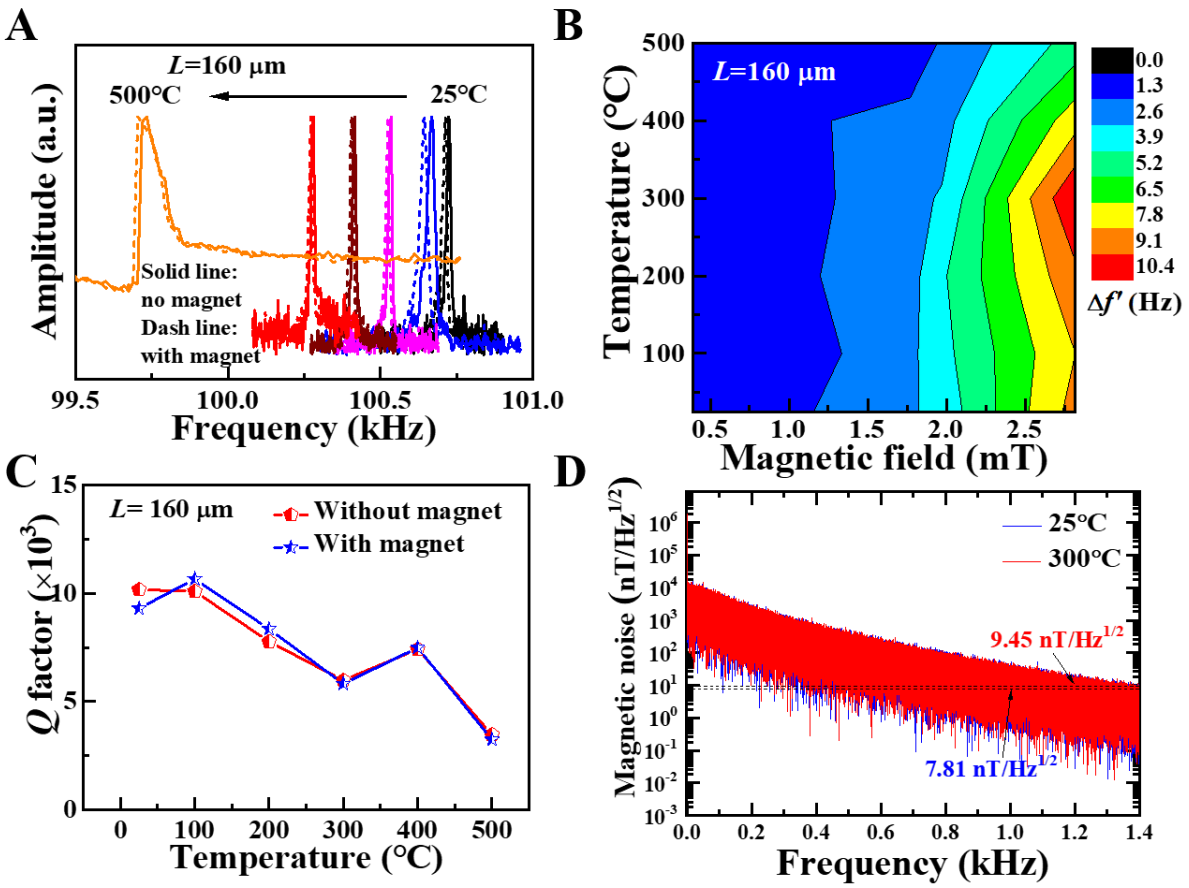

Figure 3. High-temperature magnetic transducing performance through on-chip actuation and sensing. A) Resonance frequency shift of a 160-μm-long SCD-based cantilever transducer as a function of the measurement temperature at a magnetic field of 2.82 mT, and at V_{sd}^{ac} = 4 V and V_{g}^{ac} = 7 V from 25 °C to 500 °C. The peak amplitude of the etch spectrum is normalized. B) Resonance frequency shifts of the magnetic transducer *vs.* the measurement temperature at different magnetic fields. C) *Q* factor variations of the magnetic transducer *vs.* temperature without and with applying a magnetic field of 2.82 mT. D) Magnetic noise spectra of the magnetic transducer at 25 °C and 300 °C.

Based on the high thermal stability of SCD-based cantilevers with the on-chip actuation and sensing structure, the magnetic transducing of the SCD-based magnetic transducers from 25 °C to 500 °C was realized through the Δ*E* effect. The dependence of the resonance frequency shift on the magnetic field was utilized to indicate the magnetic sensitivity of the SCD-based transducer. The magnetic sensitivity is defined as $\Delta f' = |f_{r0}-f_{rH}|$, where f_{rH} and f_{r0} represent the resonance frequencies of the SCD-based transducer with and without the magnetic field, respectively. **Figure 3a** shows the resonance frequency spectra shift of the 160-μm-long SCD-

based magnetic transducer caused by applying a magnetic field of 2.82 mT with the temperature increasing from 25 °C to 500 °C. The resonance frequency shifted as a function of the magnetic fields tuned via temperature (**Figure 3b**). The resonance frequency shift increased with the magnetic field. The SCD-based magnetic transducer with on-chip actuation and sensing exhibited a stable magnetic sensitivity of 3.2 Hz/ mT at various temperatures. Therefore, the on-chip SCD MEMS magnetic sensor with all-electrical actuation and sensing is robust at high temperatures up to 500 °C. Another SCD-based transducer demonstrates similar magnetic sensing performances (**Figure S5, Supporting Information**). To some extent, the Q factors of the SCD-based magnetic transducer decreased as temperature increased (**Figure 3c**). However, the overall magnetic sensing performance did not change significantly as the temperature increased. In addition, the magnetic noise spectra resulting from the thermomechanical noise of the SCD-based magnetic transducer were measured at 25 °C and 300 °C, as shown in **Figure 3d**. The magnetic noise levels of the SCD-based magnetic transducer reached a low level of 7.81 nT/Hz$^{1/2}$ at 25 °C and 9.45 nT/Hz$^{1/2}$ at 300 °C. For the MEMS magnetic transducer with the oscillator structure, the intrinsic magnetic noise (b_n) can be expressed as[63, 64]

$$b_n = \frac{1}{2}\mu_0 \frac{dH}{df}\sqrt{\frac{2\pi k_B T f_{r_0}}{QV\sigma'}}b_n, \quad (8)$$

which is utilized to predict the theoretical magnetic noise at the resonant frequency f_{r0}. Here, $\mu_0(\mathrm{d}H/\mathrm{d}f)$ is the magnetic sensitivity of the magnetic transducer, T the temperature, and V the device volume. The stress, σ', is calculated from f_{r0}, which is discussed in our previous publication.[27] Based on the magnetic sensing performance of the 160-μm-long on-chip magnetic transducer, the intrinsic magnetic noises of the magnetic sensor were estimated as 0.632 nT/Hz$^{1/2}$ at 25 °C, 0.825 nT/Hz$^{1/2}$ at 300 °C, and 1.09 nT/Hz$^{1/2}$ at 500 °C. Additionally, the Allan deviation of the SCD-based magnetic transducer was investigated (**Figure S6, Supporting Information**). The minimum fluctuation of the resonance frequency up to 300 °C was 2.3 × 10^{-6}. Based on the magnetic sensitivity, the minimum detectable magnetic fields for

the SCD-based magnetic transducer were calculated to be 2.02×10^{-11} T (20.2 pT) and 3.47×10^{-11} T (34.7 pT) at 300 K and 773 K, respectively. Meanwhile, based on the stable magnetic sensitivity, high Q factors result in low magnetic noise levels. To improve the magnetic sensitivity of the SCD-MEMS magnetic transducer, smaller thickness of tens of nanometers in SCD resonators is preferred. However, for high-speed response, high-frequency resonators with shorter length (i.e. micrometer scale) are desirable. A larger thickness of the FeGa film is favorable as well, but a trade-off with the Q factor should be considered. The high-temperature magnetic sensing performances of various representative high-temperature magnetic sensors were compared with those of the present sensor in terms of magnetic sensitivity, magnetic noise, and thermal stability, as summarized in **Table 1**. The on-chip magnetic sensor in this study exhibits superior sensitivity, lower noise level, and higher thermal reliability compared with other magnetic sensors.

Table 1. High-temperature sensing performance comparison of various high-temperature magnetic sensors.

Magnetic sensor	Materials	Magnetic sensitivity	Noise level	Operating temperature	Stable operating duration	Ref.
AMR	Si-based	--	~2.6 nT/Hz$^{1/2}$	498 K	>2000 h	[65]
Hall	Si	--	>82 nT/Hz$^{1/2}$	673 K	--	[66]
Hall	AlGaN/ GaN	--	35 μT/√Hz$^{1/2}$	873 K	--	[67]
Hall	4H-SiC	80 V/(A·T)	--	770 K	--	[68]
Fluxgate	Cu coil	--	0.79 nT/Hz$^{1/2}$	523 K	>100 h	[26]
MEMS	FeGa/Ti/ SCD	3.2 Hz/mT	9.45 nT/Hz$^{1/2}$	573 K	>100 h	This study

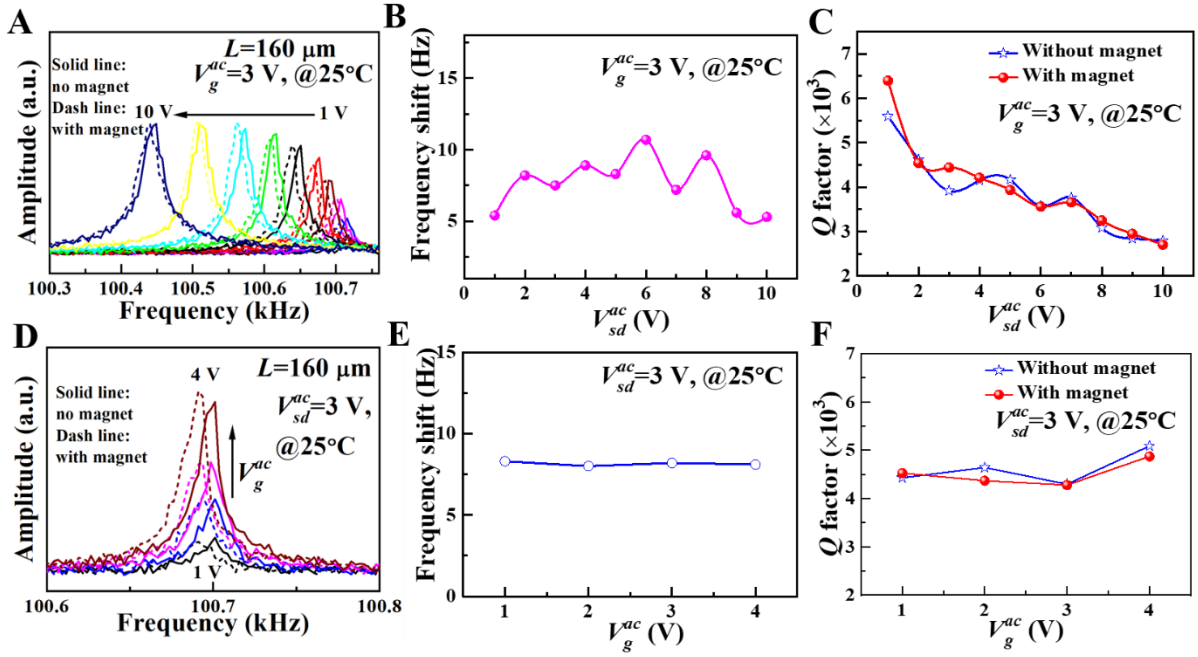

Figure 4. Magnetic transducing performances with changing V_{sd}^{ac} and V_g^{ac} at room temperature. A) Resonance frequency spectra of a 160 μm-long SCD-based magnetic transducer response to a magnetic field of 2.82 mT by changing V_{sd}^{ac} at V_g^{ac} = 3 V. B) Tuning of resonance frequency shift of the magnetic transducer *via* V_{sd}^{ac} under a magnetic field of 2.82 mT at V_g^{ac} = 3 V. C) Dependence of *Q* factors of the magnetic transducer on V_{sd}^{ac} without and with a magnetic field of 2.82 mT. V_g^{ac} is fixed at 3 V. D) Resonance frequency spectra of the magnetic transducer response to a magnetic field of 2.82 mT by changing V_g^{ac} at V_{sd}^{ac} = 3 V. E) Resonance frequency shifts of the magnetic transducer as a function of V_g^{ac} under a magnetic field of 2.82 mT at V_{sd}^{ac} = 3 V. F) Variation in *Q* factors of the magnetic transducer as V_g^{ac} without and with a magnetic field of 2.82 mT. V_{sd}^{ac} is fixed at 3 V.

The effects of V_{sd}^{ac} and V_g^{ac} on the the magnetic sensing performance of the on-chip magnetic transducer are investigated. **Figure 4a** shows the dependences of the resonance frequency spectra shift of the SCD-based magnetic transducer on V_{sd}^{ac} with or without applying a magnetic field (H = 2.82 mT) at 25 °C and V_g^{ac} =3 V. The solid and dashed lines represent the resonance frequency spectra without and with the application of the magnetic field, respectively. Although the resonance amplitude increased with V_{sd}^{ac}, the resonance frequency of the on-chip magnetic transducer was barely affected by V_{sd}^{ac} (**Figure 4b**) under a magnetic field. The *Q* factors of the on-chip magnetic transducer without and with the magnetic field decreased as V_{sd}^{ac} increased

(**Figure 4c**). The possible reasons have been discussed in the previous section. Thus, a suitable V_{sd}^{ac} should be selected with regard to two aspects: (1) a sufficient voltage to achieve a high signal readout and (2) minimal impact on the Q factor. **Figure 4d** shows the effect of V_g^{ac} on the resonance frequency shift of the on-chip transducer with or without the application of a magnetic field (H = 2.82 mT) at 25 °C and V_{sd}^{ac} = 3 V. Similarly, the amplitude of the resonance frequency with and without the application of the magnetic field increased with V_g^{ac}, as shown in **Figure 4e**. V_g^{ac} did not significantly affect the resonance frequency shift or Q factor when the magnetic field was applied, as shown in **Figures 4e and f**.

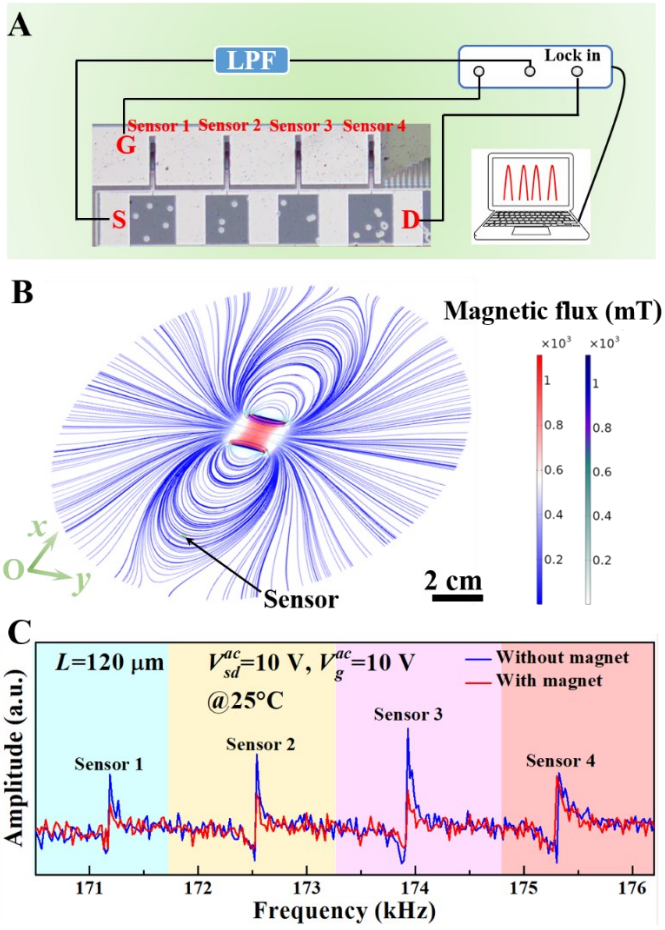

Figure 5. Magnetic transducing of a transducer array. A) Measurement setup for an SCD-based magnetic transducer array with the on-chip actuation and sensing configuration. The length and width of each cantilever sensor were 120 and 10 μm, respectively. B) The magnetic flux density in the *xoy* plane of a cylindrical magnet is simulated using the COMSOL software. The magnetization of this magnet merely occurs in the *y*-axis direction, showing a magnetic susceptibility of 1032000 A/m. The height and radius of the cylindrical magnet were 2 and 1

cm, respectively. C) Resonance frequency spectra shifts of the magnetic transducer array due to the application of a 2.82 mT magnetic field at V_{sd}^{ac} = 10 V and V_{g}^{ac} = 10 V @25 °C. The magnetic transducer array comprised four SCD-based magnetic sensors.

Finally, we demonstrate an SCD-based magnetic transducer array comprising four on-chip magnetic transducers integrated on the same chip for magnetic transducing with all-electrical actuation and sensing. **Figure 5a** shows an on-chip SCD-based magnetic transducer array. COMSOL software was utilized to simulate the magnetic flux distribution of a two-dimensional plane of a cylindrical magnet (**Figure 5b**). Owing to the independent resonance vibration of each magnetic transducer, the parallel signal readout of the four magnetic transducers was realized. The resonance frequency spectra of the magnetic transducer array exhibited four peaks without and with the application of a magnetic field of 0.28 mT, respectively, as depicted in **Figure 5c**. The resonance frequencies shifted downward in the magnetic transducer array because of the ΔE effect. A view of the resonance frequency shift with the application of a magnetic field is shown in **Figure S7 (Supporting Information)**. Alternatively, applying a magnetic field exhibited a weak effect on the Q factor of each magnetic sensor in the magnetic transducer array **(Figure S7, Supporting Information**). The successful realization of the magnetic sensing of the SCD-based magnetic transducer array is a first step toward the development of robust magnetic image sensors with high sensitivity and spatial resolution.

3. **Conclusion**

In summary, we proposed and demonstrated an all-electrical on-chip diamond MEMS magnetic sensor by integrating magnetostrictive FeGa with an SCD MEMS resonator. The magnetostrictive FeGa film functioned as an actuation electrode, a sensing head for magnetic fields, and an electrical readout unit. The SCD-based MEMS magnetic transducer exhibited high-temperature operation up to 500 °C with a high-sensitivity of 3.2 Hz/mT and a low noise

level of 9.45 nT/Hz$^{1/2}$ at 300 °C. The minimum fluctuation of the resonance frequency reached 1.9×10^{-6} at room temperature and 2.3×10^{-6} at 300 °C. The prototype SCD-based MEMS magnetic transducer array was developed with the achievement of parallel signal readout. The magnetic sensing performance can be further enhanced via nanoscale size design,[69] a high quality factor,[70] and a large magneto-strictive thin film.[69, 71] The current study successfully demonstrated the integration of SCD-based MEMS magnetic transducers with electronics, which serves as a foundation toward the development of magnetic image sensors with high sensitivity, reliability, and tunable spatial resolution.

4. Experimental section

4.1 Fabrication of on-chip SCD-based cantilever transducers

The fabrication of the SCD cantilevers was begun from the homoepitaxial layers grown on the high-pressure high-temperature (HPHT) SCD substrates. Before the diamond growth, the HPHT SCD substrates were orderly cleaned in boiling mixture acids (H_2SO_4+HNO_3), acetone, ethanol, and deionized water. Then, the cleaned HPHT SCD substrates were undergone the implantation treatment of carbon ions at an energy of 180 keV and a dose of 10^{16} cm^{-2}. The diamond epilayers were grown on the HPHT SCD substrates *via* a microwave chemical vapor deposition (MPCVD) facility with growth parameters of a methane concentration of 1 %, a hydrogen flow of 500 sccm, a microwave power of 1000 W, a substrate temperature of 880°C and a growth duration of 2 h. During the diamond growth, a 200 nm-thick graphite-like layer resulted from the ion implantation was formed under the diamond surface, which was acted as a sacrificial layer to produce the cantilever structure. The structure of the graphite-like layer was characterized through a transmission electron microscopy (TEM) technique, as shown in detail in our pervious works.[72, 73] The existence of the graphite-like layer had little impact on

the crystal quality of the SCD epilayer, as disclosed by Raman spectroscopy mapping (**Figure S8, Supporting Information**). The graphite-like layer was removed through wet or dry etching to release the SCD cantilevers. Thus, the graphite-like layer has weak influence on the sensing performance of the SCD-based magnetic transducers. However, the diamond at the bottom of the cantilever was defective due to the ion implantation. To eliminate this damage, the SCD samples were annealed at 1100°C for 3 h in an ultrahigh vacuum condition (~10^{-7} Pa). However, we could not identify the damage induced by the ion-implantation through TEM and Raman. By contrast, the Q factors of the SCD cantilevers were improved after annealing at 1100°C (**Figure S9, Supporting Information**). A laser photolithographic approach was utilized to pattern the SCD samples and fabricate the SCD cantilevers.[32]

A further laser photolithography process was utilized to pattern the on-chip SCD cantilevers with the actuation and sensing structure. A 2 nm-thick Ti film followed by a 90 nm-thick FeGa film was deposited on the SCD cantilevers by a magneto sputtering system. The FeGa film was regarded as actuation electrode, magnetic transducing component, and electrical readout unit. The growth conditions of the Ti and FeGa films were: a Ar flow of 10 sccm, a working pressure of 1 Pa, a sputtering power of 100 W, and room temperature. Alternatively, a 1 nm-thick Ti film followed by a 7 nm-thick Au film was deposited on SCD cantilevers as the source, drain, and gate electrodes by an e-beam evaporator system. The SCD cantilever configuration with an actuation and sensing configuration was confirmed by an optical microscope system.

4.2 Optical and electrical readout of the mechanical resonance

The mechanical resonance properties of the SCD cantilevers without and with the deposition of films including FeGa/Ti films and Au electrodes were analyzed *via* an optical readout system with the Laser Vibormetry. The gate electrode connected to a RF signal was used to actuate the SCD cantilevers. The optical signal reflected from the vibration of the SCD

cantilevers was read out by a lock-in amplifier. The magnetic transducing performance of the SCD-based magnetic transducers with the actuation and sensing structure were measured by an electrical readout system. The G electrode was connected to a radio-frequency (RF) signal with an amplitude of V_g^{ac} and a frequency of ω to actuate the cantilevers. Another RF signal with an amplitude of V_{sd}^{ac} and a frequency of $\omega+\Delta\omega$ was applied to the S-D electrode to capture the vibrational signal. The displacement of the cantilevers led to the variation in the resistance of the S-D electrode. A reference signal, $\Delta\omega$ of 5 kHz was utilized to readout the electrical signal. The magnetic fields were applied by the different magnets to accomplish the magnetic transducing measurement. A heater below the magnetic transducer was utilized to control the temperatures from room temperature to high temperatures. The measurements were performed in a vacuum chamber with a pressure lower than 10^{-3} Pa.

Supporting Information

Supporting Information is available from the Wiley Online Library or from the author.

Acknowledgments

This work was supported by a Grant-in-Aid of JSPS KAKENHI (no. 20H02212, 22K18957, 15H03999), JSPS Research Fellowship (no. 22F21341), Bilateral joint research between JSPS (JPJSBP120227203) and CAS, and Nanotechnology Platform projects sponsored by the Ministry of Education, Culture, Sports, and Technology (MEXT) of Japan.

Conflict of Interest

The authors declare no conflict of interests.

Data Availability Statement

The data that support the findings of this study are available on request from the corresponding author.

Received: ((will be filled in by the editorial staff))

Revised: ((will be filled in by the editorial staff))

Published online: ((will be filled in by the editorial staff))

References

[1] M. Pannetier, C. Fermon, G. Le Goff, J. Simola, E. Kerr, *Science* **2004**, 304, 1648.
[2] Y. Wang, J. Li, D. Viehland, *Mater. Today* **2014**, 17, 269.
[3] L. Ichkitidze, N. Bazaev, D. Telyshev, R. Preobrazhensky, M. Gavrushina, *Biomed. Eng.* **2015**, 48, 305.
[4] D. Suess, A. Bachleitner-Hofmann, A. Satz, H. Weitensfelder, C. Vogler, F. Bruckner, C. Abert, K. Prügl, J. Zimmer, C. Huber, *Nat. Electron.* **2018**, 1, 362.
[5] W. Li, J. Wang, *The Journal of navigation* **2014**, 67, 263.
[6] U. P. Borole, S. Subramaniam, I. R. Kulkarni, P. Saravanan, H. C. Barshilia, P. Chowdhury, *Sens. Actuator A Phys.* **2018**, 280, 125.
[7] M. Hott, P. A. Hoeher, S. F. Reinecke, *Sensors* **2019**, 19, 3415.
[8] H. Grüger, *Sens. Actuator A Phys.* **2003**, 106, 326.
[9] J. Lenz, S. Edelstein, *IEEE Sens. J.* **2006**, 6, 631.
[10] X. Zhao, Y. Bai, Q. Deng, C. Ai, X. Yang, D. Wen, *IEEE Sens. J.* **2017**, 17, 5849.
[11] L. Bian, Y. Wen, Y. Wu, P. Li, Z. Wu, Y. Jia, Z. Zhu, *IEEE Trans. Electron Dev.* **2018**, 65, 2585.
[12] H. Mamin, M. Kim, M. Sherwood, C. Rettner, K. Ohno, D. Awschalom, D. Rugar, *Science* **2013**, 339, 557.
[13] M. Lesik, T. Plisson, L. Toraille, J. Renaud, F. Occelli, M. Schmidt, O. Salord, A. Delobbe, T. Debuisschert, L. Rondin, *Science* **2019**, 366, 1359.
[14] A. L. Herrera-May, L. A. Aguilera-Cortés, P. J. García-Ramírez, E. Manjarrez, *Sensors* **2009**, 9, 7785.
[15] M. Sekino, A. Kuwahata, T. Ookubo, M. Shiozawa, K. Ohashi, M. Kaneko, I. Saito, Y. Inoue, H. Ohsaki, H. Takei, *Sci. Rep.* **2018**, 8, 1.
[16] C. Lei, J. Lei, Z. Yang, T. Wang, Y. Zhou, *Microsyst. Technol.* **2013**, 19, 591.
[17] A. L. Herrera-May, J. C. Soler-Balcazar, H. Vázquez-Leal, J. Martínez-Castillo, M. O. Vigueras-Zuñiga, L. A. Aguilera-Cortés, *Sensors* **2016**, 16, 1359.
[18] F. Casola, T. Van Der Sar, A. Yacoby, *Nat. Rev. Mater.* **2018**, 3, 1.
[19] J. L. Webb, L. Troise, N. W. Hansen, J. Achard, O. Brinza, R. Staacke, M. Kieschnick, J. Meijer, J.-F. Perrier, K. Berg-Sørensen, *Frontiers Phys.* **2020**, 8, 522536.
[20] P. Maletinsky, S. Hong, M. S. Grinolds, B. Hausmann, M. D. Lukin, R. L. Walsworth, M. Loncar, A. Yacoby, *Nat. Nanotechnol.* **2012**, 7, 320.
[21] A. S. Algamili, M. H. M. Khir, J. O. Dennis, A. Y. Ahmed, S. S. Alabsi, S. S. Ba Hashwan, M. M. Junaid, *Nanoscale Res. Lett.* **2021**, 16, 1.
[22] R. T. Fingers, C. S. Rubertus, *IEEE Trans. Magn.* **2000**, 36, 3373.
[23] O. Gutfleisch, M. A. Willard, E. Brück, C. H. Chen, S. Sankar, J. P. Liu, *Adv. Mater.* **2011**, 23, 821.
[24] M. Hecker, D. Tietjen, C. Schneider, N. Cramer, L. Malkinski, R. Camley, Z. Celinski, *J. Appl. Phys.* **2002**, 91, 7203.
[25] J. Jankowski, S. El-Ahmar, M. Oszwaldowski, *Sensors* **2011**, 11, 876.
[26] D. Rühmer, S. Bögeholz, F. Ludwig, M. Schilling, *Sens. Actuators A Phys.* **2015**, 228, 118.
[27] Z. Zhang, H. Wu, L. Sang, Y. Takahashi, J. Huang, L. Wang, M. Toda, I. M. Akita, Y. Koide, S. Koizumi, *ACS Appl. Mater. Interfaces* **2020**, 12, 23155.

[28] Z. Zhang, Y. Wu, L. Sang, H. Wu, J. Huang, L. Wang, Y. Takahashi, R. Li, S. Koizumi, M. Toda, *Mater. Res. Lett.* **2020**, 8, 180.

[29] H. J. Kim, S. Wang, C. Xu, D. Laughlin, J. Zhu, G. Piazza, 30th Int. Conf. Micro Electr. Mech. Syst. (MEMS) **2017**.

[30] A. Banerjee, D. Bernoulli, H. Zhang, M.-F. Yuen, J. Liu, J. Dong, F. Ding, J. Lu, M. Dao, W. Zhang, *Science* **2018**, 360, 300.

[31] C. Dang, J.-P. Chou, B. Dai, C.-T. Chou, Y. Yang, R. Fan, W. Lin, F. Meng, A. Hu, J. Zhu, *Science* **2021**, 371, 76.

[32] M. Liao, *Functional Diamond* **2022**, 1, 29.

[33] G. Shu, B. Dai, A. Bolshakov, W. Wang, Y. Wang, K. Liu, J. Zhao, J. Han, J. Zhu, *Functional Diamond* **2022**, 1, 47.

[34] T. Bautze, S. Mandal, O. A. Williams, P. Rodiere, T. Meunier, C. Bäuerle, *Carbon* **2014**, 72, 100.

[35] M. Liao, S. Hishita, E. Watanabe, S. Koizumi, Y. Koide, *Adv. Mater.* **2010**, 22, 5393.

[36] B. A. Fairchild, S. Rubanov, D. W. Lau, M. Robinson, I. Suarez-Martinez, N. Marks, A. D. Greentree, D. McCulloch, S. Prawer, *Adv. Mater.* **2012**, 24, 2024.

[37] B. A. Fairchild, P. Olivero, S. Rubanov, A. D. Greentree, F. Waldermann, R. A. Taylor, I. Walmsley, J. M. Smith, S. Huntington, B. C. Gibson, *Adv. Mater.* **2008**, 20, 4793.

[38] H. Sun, L. Sang, H. Wu, Z. Zhang, T. Teraji, T.-F. Li, J. You, M. Toda, S. Koizumi, M. Liao, *Phys. Rev. Lett.* **2020**, 125, 206802.

[39] B. Regan, A. Aghajamali, J. Froech, T. T. Tran, J. Scott, J. Bishop, I. Suarez-Martinez, Y. Liu, J. M. Cairney, N. A. Marks, *Adv. Mater.* **2020**, 32, 1906458.

[40] M. Malakoutian, X. Zheng, K. Woo, R. Soman, A. Kasperovich, J. Pomeroy, M. Kuball, S. Chowdhury, *Adv. Funct. Mater.* **2022**, 2208997.

[41] O. Auciello, *Functional Diamond* **2022**, 2, 1.

[42] N. Yang, S. Yu, J. V. Macpherson, Y. Einaga, H. Zhao, G. Zhao, G. M. Swain, X. Jiang, *Chem. Soc. Rev.* **2019**, 48, 157.

[43] J. Atulasimha, A. B. Flatau, *Smart Mater. Struct.* **2011**, 20, 043001.

[44] T. Ma, J. Gou, S. Hu, X. Liu, C. Wu, S. Ren, H. Zhao, A. Xiao, C. Jiang, X. Ren, *Nat. Commun.* **2017**, 8, 1.

[45] M. Liao, S. Sang, T.Teraji, S. Koizumi, Y. Koide, *Adv. Mater. Technol*. **2019**, 4, 1800325.

[46] D. Y. Park, D. J. Joe, D. H. Kim, H. Park, J. H. Han, C. K. Jeong, H. Park, J. G. Park, B. Joung, K. J. Lee, *Adv. Mater.* **2017**, 29, 1702308.

[47] V. Sazonova, Y. Yaish, H. Üstünel, D. Roundy, T. A. Arias, P. L. McEuen, *Nature* **2004**, 431, 284.

[48] C. Chen, S. Rosenblatt, K. I. Bolotin, W. Kalb, P. Kim, I. Kymissis, H. L. Stormer, T. F. Heinz, J. Hone, *Nat. Nanotechnol.* **2009**, 4, 861.

[49] R. He, X. Feng, M. Roukes, P. Yang, *Nano Lett.* **2008**, 8, 1756.

[50] Y.-I. Sohn, M. J. Burek, V. Kara, R. Kearns, M. Lončar, *Appl. Phys. Lett.* **2015**, 107, 243106.

[51] Z. Zhang, H. Wu, L. Sang, J. Huang, Y. Takahashi, L. Wang, M. Imura, S. Koizumi, Y. Koide, M. Liao, *Carbon* **2019**, 152, 788.

[52] M. Liao, M. Toda, L. Sang, T. Teraji, M. Imura, Y. Koide, *Jpn. J. Appl. Phys.* **2017**, 56, 024101.

[53] W. Weaver Jr, S. P. Timoshenko, D. H. Young, *Vibration problems in engineering*, John Wiley & Sons, **1991**.

[54] M. Bao, *Analysis and design principles of MEMS devices*, Elsevier, **2005**.

[55] I. Bargatin, E. Myers, J. Arlett, B. Gudlewski, M. Roukes, *Appl. Phys. Lett.* **2005**, 86, 133109.

[56] H. Wu, Z. Zhang, L. Sang, T. Li, J. You, Y. Lu, Y. Koide, M. Liao, *Diamond Relat. Mater.* **2020**, 103, 107711.
[57] B. Gojdka, R. Jahns, K. Meurisch, H. Greve, R. Adelung, E. Quandt, R. Knöchel, F. Faupel, *Appl. Phys. Lett.* **2011**, 99, 223502.
[58] I. Chopra, J. Sirohi, *Smart structures theory*, Cambridge University Press, **2013**.
[59] J. Rieger, T. Faust, M. J. Seitner, J. P. Kotthaus, E. M. Weig, *Appl. Phys. Lett.* **2012**, 101, 103110.
[60] F. Aguilar Sandoval, M. Geitner, É. Bertin, L. Bellon, *J. Appl. Phys.* **2015**, 117, 234503.
[61] H. A. Tilmans, M. Elwenspoek, J. H. Fluitman, *Sens. Actuators A Phys.* **1992**, 30, 35.
[62] M. Toda, N. Inomata, T. Ono, I. Voiculescu, *IEEJ Trans. Electr. Electron. Eng.* **2017**, 12, 153.
[63] S. Bennett, J. Baldwin, M. Staruch, B. Matis, J. LaComb, O. J. van't Erve, K. Bussmann, M. Metzler, N. Gottron, W. Zappone, *Appl. Phys. Lett.* **2017**, 111, 252903.
[64] J. Kiser, R. Lacomb, K. Bussmann, C. J. Hawley, J. E. Spanier, X. Zhuang, C. Dolabdjian, S. Lofland, P. Finkel, *Appl. Phys. Lett.* **2014**, 104, 072408.
[65] B. B. Pant, L. Withanawasam, M. Bohlinger, M. Larson, B. W. Ohme, *J. Microelectron. Electron. Packag.* **2015**, 12, 205-211.
[66] R. S. Popovic, *In Proc. 29th Int. Conf. Microelectron. (MIEL)*, May 2014, pp. 69–74.
[67] T. Yamamura, D. Nakamura, M. Higashiwaki, T. Matsui, A. Sandhu, *J. Appl. Phys.* **2006**, 99, 08B302.
[68] T. Ciuk, B. Stanczyk, K. Przyborowska, D. Czolak, A. Dobrowolski, J. Jagiello, W. Kaszub, M. Kozubal, R. Kozlowski, P. Kaminski, *IEEE Trans. Electron Dev.* **2019**, 66, 3134.
[69] M. Li, A. Matyushov, C. Dong, H. Chen, H. Lin, T. Nan, Z. Qian, M. Rinaldi, Y. Lin, N. X. Sun, *Appl. Phys. Lett.* **2017**, 110, 143510.
[70] Y. Tao, J. M. Boss, B. Moores, C. L. Degen, *Nat. Commun.* **2014**, 5, 1.
[71] Z. Zhang, L. Sang, J. Huang, W. Chen, L. Wang, Y. Takahashi, S. Mitani, Y. Koide, S. Koizumi, M. Liao, *Carbon* **2020**, 170, 294.
[72] M. Liao, Y. Koide, L. Sang, in *Novel Aspects of Diamond: From Growth to Applications*, Springer International Publishing, Cham **2019**.
[73] M. Liao, M. Toda, L. Sang, S. Hishita, S. Tanaka, Y. Koide, *Appl. Phys. Lett.* **2014**, 105, 251904.